

Research



Cite this article: Vara Prasad GVV, Kumar P, Dhar P, Samanta D. 2025 Fluid dynamics of droplet impact and splitting on superhydrophobic wedges. *Proc. R. Soc. A* **481**: 20240525.

<https://doi.org/10.1098/rspa.2024.0525>

Received: 18 July 2024

Accepted: 30 January 2025

Subject Category:

Engineering

Subject Areas:

chemical engineering, mechanical engineering, fluid mechanics

Keywords:

droplets, superhydrophobicity, wedges, volume of fluid (VOF), dynamic contact angle, Kistler model, OpenFOAM

Author for correspondence:

Purbarun Dhar

e-mail: purbarun@mech.iitkgp.ac.in

Fluid dynamics of droplet impact and splitting on superhydrophobic wedges

Gudlavalleti V. V. S. Vara Prasad^{1,2}, Parmod Kumar², Purbarun Dhar³ and Devranjan Samanta¹

¹Department of Mechanical Engineering, Indian Institute of Technology Ropar, Punjab 140001, India

²Indian Institute of Technology Mandi, Himachal Pradesh 175075, India

³Hydrodynamics and Thermal Multiphysics Lab, Department of Mechanical Engineering, Indian Institute of Technology Kharagpur, West Bengal 721302, India

PD, 0000-0001-5473-2993; DS, 0000-0002-3406-1472

We report an extensive computational and experimental investigation of droplet impact and subsequent splitting hydrodynamics on superhydrophobic wedges. Using two-dimensional (2D) and three-dimensional (3D) volume-of-fluid (VOF) simulations, supported by high-speed imaging experiments, we predict the impact, spreading, splitting, retraction and daughter droplet lift-off from superhydrophobic wedges. In particular, we examine how the wedge angle (ϕ), wedge asymmetry ($\phi_1 - \phi_2$), Weber number (We) and normalized Bond number (Bo^*) influence the post-impact dynamics. We observe that for symmetric wedges, the maximum spread factor (β)_{max} of the droplet decreases with an increase in wedge angle (ϕ) at a fixed We . At high wedge angles, the sharp steepness of the wedge causes less contact area for the droplet to spread. For the asymmetric wedges, it has been noted that (β)_{max} increases with an increase in We owing to the higher inertial forces of the droplet against sliding. Furthermore, (β)_{max} increases with an increase in Bo^* at a fixed We owing to the dominance of the gravitational force over the capillary force of the droplet. It has also been found that at the same Bo^* , (β)_{max} rises with an increase in We owing to the dominance of inertial forces over capillary forces. We discuss the non-dimensional split volume (V) of daughter droplets during the split-up stage for

different symmetric and asymmetric wedge angles. In general, our 2D simulations agree well with the experiments for a major part of the droplet's lifetime. Further, we have conducted a detailed 3D simulation-based energy-budget analysis to estimate the temporal evolution of the various energy components at different post-impact hydrodynamic regimes.

1. Introduction

Droplet impact on solid surfaces [1] has broad implications in a wide variety of applications; viz. inkjet printing [2–6], spray coating and painting [7], spray cooling [8–11] and anti-icing [12]. Consequently, studies focusing on the allied transport phenomena of droplet impacts and their outcomes involving experiments, theory and computer simulations have been widely reported in the literature. Given the large range of physical insights available from detailed simulations, particularly using the volume-of-fluid (VOF) method [13–16], several research teams have made significant contributions to the underlying physics of droplet spreading, deformation, fragmentation, rebound and recoil on solid surfaces of different wettabilities.

For instance, Hu *et al.* [17] demonstrated that micro droplets impacting structured superhydrophobic surfaces experience higher Laplace pressure compared with macro droplets, leading to increased wetting pressure during the impalement event. Expanding on this, Debnath *et al.* [18,19] explored the spreading dynamics of highly viscous droplets on superhydrophobic surfaces, highlighting the dominant influence of viscosity with minimal inertia effects. Their further studies [20] showed how surface inclination significantly reduces droplet contact time. Henman *et al.* [21] investigated early transients of droplet impact dynamics on textured and lubricant-infused surfaces, showing reduced splash jet range with increased surface asperity spacing.

Focusing on contact-angle dynamics, Vontas *et al.* [22] demonstrated the capability of Kistler's dynamic contact-angle model in capturing droplet spreading, recoiling and rebound dynamics during the post-impact phase of droplets on smooth surfaces. Malgarinos *et al.* [23] reviewed contact-angle dynamics during droplet spreading, focusing on different models ranging from standard to non-wetting models. Their comparison showed consistent results, except for Shikhmurzaev's dynamic contact-angle model, which frequently yielded more accurate spreading ratio predictions. Zhang *et al.* [24] combined molecular dynamics and VOF approaches for molecular dynamics simulations, emphasizing the insufficiency of dynamic contact angles alone in capturing nanodroplet wetting behaviours. They concluded that dynamic contact-angle information alone is insufficient to capture molecular-level effects during wetting. The geometric influence on droplet impact has also been extensively studied. Liu *et al.* [25,26] studied droplet impact on spherical and concave surfaces, finding good agreement with experiments and noting distinctive spreading dynamics such as maximum spread factor and area based on surface geometry. Ding *et al.* [27] utilized the VOF method to study droplet breakup and rebound dynamics during droplet impact on small cylindrical superhydrophobic targets. They observed that increasing Weber number (We) accelerated droplet spreading and promoted breakup. Luo *et al.* [28] extended this approach to explore droplet impact on conical surfaces, finding a remarkable approximately 54% reduction in contact time during the phase where the droplet lifted off as a ring, compared with impacts on flat surfaces.

Other studies have highlighted additional factors influencing droplet behaviour. Wasserfall *et al.* [29] examined coalescence-induced droplet jumping on superhydrophobic surfaces, showing that a smaller size ratio between merging droplets enhances the adhesion force-to-energy ratio, leading to more efficient energy transfer during coalescence. Similarly, Russo *et al.* [30] investigated droplet dynamics on wettability-patterned surfaces, employing the Kistler contact-angle model. Their simulations closely matched experimental results, particularly in

predicting droplet translation, splitting and vectoring behaviours, including non-orthogonal rebound of droplets impacting orthogonally on a superhydrophobic domain. Wang *et al.* [31] simulated the droplet impact on a mesh array and investigated the effect of liquid properties on impact, penetration and fragmentation using the lattice Boltzmann method. Hao *et al.* [32] examined droplet splashing dynamics on an inclined surface and demonstrated that splashing could be entirely suppressed by either increasing the surface inclination angle or reducing the ambient pressure. Zhao *et al.* [33] focused on the oblique impact of droplets on horizontal solid surfaces. They showed that impact velocity strongly affects the spreading area and droplet kinetics. In addition, their study emphasized the role of tangential velocity, demonstrating that higher tangential components lead to increased viscous dissipation, significantly influencing the post-impact behaviour of droplets.

Despite numerous investigations on droplet impact on various superhydrophobic surfaces, including flat, spherical, cylindrical and conical geometries [25–28], the specific hydrodynamic behaviour of droplets impacting superhydrophobic wedges remains largely unexplored. This gap presents a significant scientific opportunity, as studying droplet impact on superhydrophobic wedges is not only novel but also critical for advancing our understanding of fluid dynamics in complex geometries. The distinct post-impact behaviour on wedges, particularly the inevitable splitting of droplets into daughter droplets, introduces unique challenges and opportunities. Unlike flat or spherical surfaces, where droplets typically spread or rebound, the wedge geometry dictates a fundamental shift in behaviour. The symmetry or asymmetry of droplet splitting is directly influenced by the wedge geometry, creating a complex interplay between the wedge angle, surface curvature and the hydrodynamic forces at play. This splitting mechanism, especially in asymmetric wedges, introduces novel fluid dynamics phenomena that have not been captured in previous studies, offering fertile ground for new insights into the role of geometry, velocity and pressure conditions in droplet behaviour. The geometry, velocity and pressure conditions that influence the nature and evolution of the split may add important mechanics to the rich physics of droplets and their interactions with obstacles.

To address these challenges, we have conducted comprehensive simulations of droplet impacts on superhydrophobic wedges using the VOF method, supported by high-speed imaging experiments for validation. Our 3D simulations provide a detailed and comprehensive understanding of the dynamic events occurring during and after droplet splitting. The main aim of this study is to investigate the droplet spreading behaviour, split-up dynamics, fluctuations in impact forces and the distribution of various energy components during the post-impact stage on wedge surfaces. To achieve this, we simulated droplet impact dynamics on superhydrophobic wedges using the VOF method, supported by detailed experiments. To ensure greater accuracy, we performed 3D simulations, particularly capturing events during and after splitting. Our investigation thoroughly examines the effects of various factors on droplet impact behaviour, including the wedge angle (ϕ), wedge base angles (ϕ_1 , ϕ_2) and their asymmetry ($\phi_1 - \phi_2$), impact Weber number (We) and normalized Bond number (Bo^*). In addition, we incorporate energy-budget estimations and track the impact-force history during the post-impact phase, analysing droplet splitting hydrodynamics to explain the observed outcomes.

2. Simulation methodology

(a) Governing equations

We have simulated the interaction between a liquid–gas (water–air) droplet pair during the process of droplet impact on a stationary superhydrophobic wedge. The simulation of the post-impact dynamics of the droplet is dealt with in two distinct phases. As the interface separates the two phases, it is essential to choose an appropriate interface-tracking method. Despite the various possible numerical techniques available, such as the two-fluid method,

level-set method and VOF method, the VOF method (Hirt & Nichols [13]) has been adopted owing to its higher accuracy in capturing interface evolution and deformation. The governing equations to be solved are as follows:

$$\nabla \cdot \mathbf{V} = 0, \quad (2.1)$$

$$\frac{\partial \alpha}{\partial t} + \nabla \cdot (\alpha \mathbf{V}) = 0, \quad (2.2)$$

$$\rho \left[\frac{D\mathbf{V}}{Dt} \right] = -\nabla p + \nabla \cdot \mu [(\nabla \mathbf{V}) + (\nabla \mathbf{V})^T] + \rho \mathbf{g} + \mathbf{F}_{st}, \quad (2.3)$$

where \mathbf{V} , ρ , p , μ , \mathbf{g} , \mathbf{F}_{st} and α represent the velocity, density, pressure, dynamic viscosity of the fluid, gravitational acceleration, volumetric surface tension force and phase volume fraction, respectively.

In this context, the liquid volume fraction (α_l) and the corresponding gas volume fraction (α_g) within each control volume are expressed as follows:

$$\alpha_i = \begin{cases} 0 & \text{if the cell is occupied by only gas (air),} \\ 0 < \alpha_i < 1 & \text{if the cell contains both gas (air) and liquid (water),} \\ 1 & \text{if the cell is occupied by only liquid (water)} \end{cases} \quad (2.4)$$

and

$$\alpha_l + \alpha_g = 1. \quad (2.5)$$

The physical properties of the mixture are determined as a weighted average based on α . The density and viscosity of the equivalent fluid are obtained as

$$\rho = \alpha_l \rho_l + (1 - \alpha_l) \rho_g, \quad (2.6)$$

$$\mu = \alpha_l \mu_l + (1 - \alpha_l) \mu_g, \quad (2.7)$$

where ρ_l , μ_l are the density and viscosity of the liquid phase, and ρ_g , μ_g are the density and viscosity of the gaseous phases, respectively.

The VOF method incorporates a customized interface compression scheme, wherein a supplementary convective term is introduced to the transport equation of the volume fraction as follows:

$$\frac{\partial \alpha}{\partial t} + \nabla \cdot (\alpha \mathbf{V}_l) = 0, \quad (2.8)$$

$$\frac{\partial (1 - \alpha)}{\partial t} + \nabla \cdot ((1 - \alpha) \mathbf{V}_g) = 0, \quad (2.9)$$

$$\mathbf{V} = \alpha \mathbf{V}_l + (1 - \alpha) \mathbf{V}_g. \quad (2.10)$$

The velocity of the equivalent fluid is determined by assuming it to be the weighted average based on the volume fraction as

$$\frac{\partial \alpha}{\partial t} + \nabla \cdot (\alpha \mathbf{V}) + \nabla \cdot (\alpha(1 - \alpha)(\mathbf{V}_l - \mathbf{V}_g)) = 0. \quad (2.11)$$

In equation (2.3), the volumetric surface tension force \mathbf{F}_{st} acting at the liquid–gas interface is obtained from the continuum surface model [14] as

$$\mathbf{F}_{st} = \gamma k \nabla \alpha, \quad (2.12)$$

$$k = -\nabla \cdot \left(\frac{\nabla \alpha}{|\nabla \alpha|} \right), \quad (2.13)$$

where k is the mean curvature of the interface. The final form of the momentum equation is

$$\rho \left[\frac{D\mathbf{V}}{Dt} \right] = -\nabla p + \nabla \cdot \mu [(\nabla \mathbf{V}) + (\nabla \mathbf{V})^T] + \rho \mathbf{g} - \gamma \nabla \cdot \left(\frac{\nabla \alpha}{|\nabla \alpha|} \right) \nabla \alpha. \quad (2.14)$$

The discretized form of equations (2.1), (2.11) and (2.14), were solved using the open-source library OpenFOAM. To handle the pressure–velocity coupling, the PIMPLE algorithm [34] was employed in combination with adaptive time stepping, which is based on the Courant–Friedrichs–Lewy condition.

(b) Dynamic contact-angle model

To accurately predict the shape of the interface in the vicinity of the three-phase contact line, the unit normal to the interface, denoted as \mathbf{n} , is expressed as a function of the dynamic contact angle θ_d as

$$\mathbf{n} = \frac{\nabla\gamma}{|\nabla\gamma|} = \mathbf{n}_w \cos\theta_d + \mathbf{n}_t \sin\theta_d, \quad (2.15)$$

where \mathbf{n}_w and \mathbf{n}_t are the unit vectors of the solid surface in the normal and tangential directions, respectively. The contact angle varies owing to contact-angle hysteresis ($\theta_A - \theta_R$), resulting in a dynamic contact angle influenced by various factors such as droplet fluid properties, contact-line velocity, substrate characteristics and fluid–surface interactions. Several established contact-angle models, such as Shikmurzaev’s model [15], Cox’s model [16] and Kistler’s model [35] are widely used to predict the dynamic contact angle during the spreading or retracting of a droplet. The contact-angle model by Kistler has been incorporated into the VOF solver within the OpenFOAM library, and has been used in this study. Kistler’s model is described as

$$\theta_d = f_H(Ca + f_H^{-1}(\theta)), \quad (2.16)$$

where

$$f_H = \cos^{-1}\left(1 - 2\tanh\left(5.16\left(\frac{\tau}{1 + 1.31\tau^{0.99}}\right)^{0.706}\right)\right). \quad (2.17)$$

The Kistler model (equations (2.16) and (2.17)) describes the dynamic contact angle (θ_d) manifestation in terms of the contact-line velocity (u_{cl}) and dynamic wetting process. The term θ_d is expressed as a function of the dynamic contact-line capillary number ($Ca = \frac{\mu u_{cl}}{\sigma}$) and the Hoffmann function (f_H). While implementing the Kistler model, θ_d is estimated based on the value of u_{cl} , as

$$\theta = \begin{cases} \theta_A, & \text{if } u_{cl} > 0, \\ \theta_E, & \text{if } u_{cl} = 0, \\ \theta_R, & \text{if } u_{cl} < 0, \end{cases} \quad (2.18)$$

where θ_A , θ_E and θ_R represent the advancing contact angle, static equilibrium contact angle and receding contact angle, respectively. The Kistler model is preferred for its precise prediction of contact-line motion. There are certain limitations associated with its use, as it is only applicable within a specific Ca range. Moreover, the bulk motion of the contact line is truly multi-scale. A more accurate prediction of the contact-line velocity would require a molecular perspective. Nevertheless, for the length scale of the droplet in the current study, the combination of the Kistler model and the VOF method have been shown to be very accurate in estimating the contact-line dynamics [35–37].

(c) Simulation domain and grid independence test

A spherical deionized water droplet of pre-impact diameter, D_0 (2.04–3.5 mm), was allowed to impact the apex of a stationary superhydrophobic wedge at different impact velocities U_0 (refer to figure 1a for schematic). The sizes of the two-dimensional (2D) simulation domain, $b \times h$ ($b = 6.5D_0$ and $h = 6.5D_0$), were carefully chosen to avoid any boundary effects on the

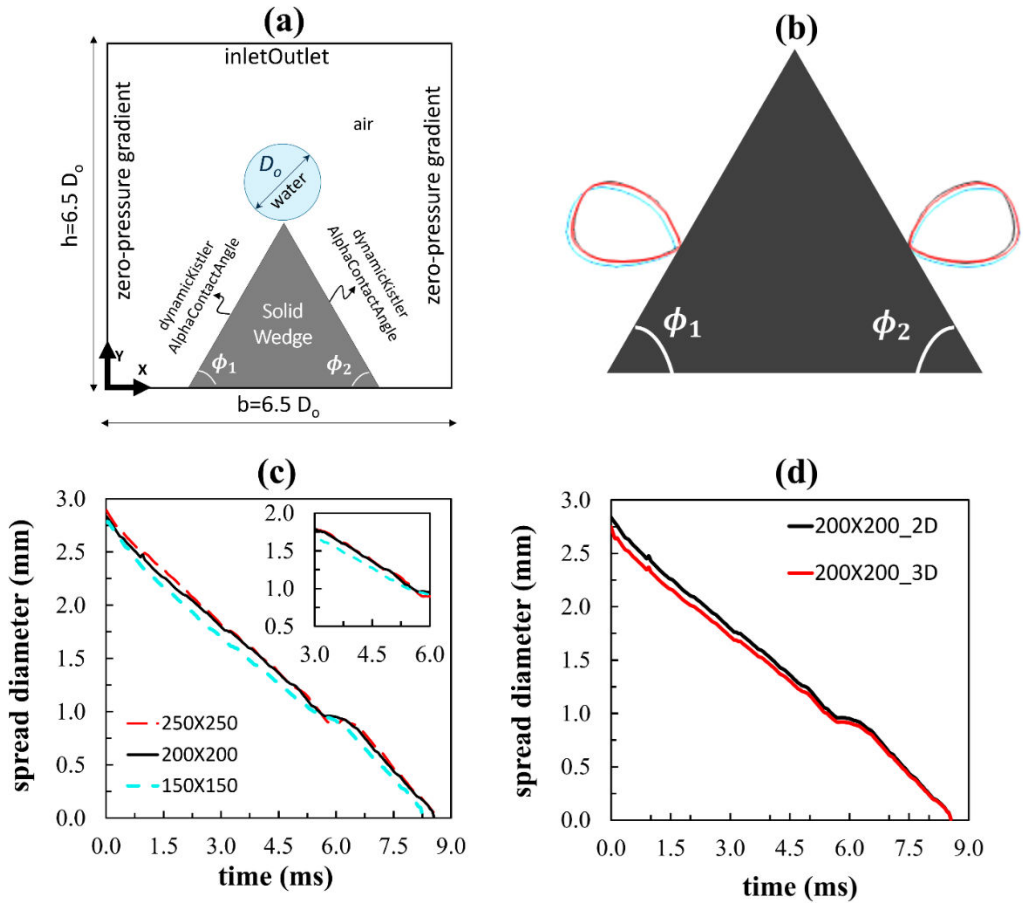


Figure 1. (a) Schematic of the 2D view of the simulation domain of a droplet impact on the apex of a stationary superhydrophobic wedge. (b) Variation in the shape of the droplet interface profile during daughter droplets lift-off event for different grids as in the legend of image c. (c) 2D grid independence test for different grid sizes for $\phi_1 = \phi_2$. (d) Variation in spreading diameter of the droplet for both 2D and 3D simulations for an optimal grid size of 200×200 .

hydrodynamics. Both symmetric and asymmetric superhydrophobic wedges, with different wedge angles (ϕ), ranging from 45° to 75° were studied in detail. An inlet–outlet boundary condition was implemented at the top wall of the domain to keep it open to ambient conditions. A zero-pressure gradient was imposed on both side walls of the domain. In addition, on the surface of the wedge and its associated bottom wall, the Kistler dynamic contact-angle model was employed. To impart superhydrophobic properties to the wedge, θ_A and θ_R were assigned values of 154° and 144° , respectively, based on current experiments. These values were chosen to minimize the contact-angle hysteresis ($CAH = \theta_A - \theta_R = 10^\circ$) in accordance with Kistler’s [35] model. These specific values were obtained from commercial spray-coated superhydrophobic surfaces. We studied the role of a droplet diameter, within the range $D_o = 2.04\text{--}3.5$ mm.

We used a structured Cartesian uniform grid to discretize the simulation domain. Various grid sizes were considered in the simulation to obtain grid-independent results. Figure 1c illustrates the temporal evolution of the droplet spreading diameter for different grid sizes. Comparing the spreading diameter values between grid sizes of 200×200 and 250×250 , it was evident that the difference is significantly small; less than $6\text{ }\mu\text{m}$ at equilibrium. The difference between grid sizes of 150×150 and 200×200 was higher, approximately $22\text{ }\mu\text{m}$ at equilibrium. Thereby, considering the spreading diameter for both the grid resolutions, the 200×200 grid

was selected as the optimal configuration for the simulations. In addition, during the lift-off stage from the wedge slopes (refer to [figure 1b](#)), the shape of the droplet interface profile was tested for different grid sizes. It was observed that the results for both 200×200 and 250×250 grid sizes overlap almost perfectly, while a significant deviation was observed between the 150×150 and 200×200 (refer to [figure 1b](#)). Hence, the 200×200 grid was justified. Further, we conducted a thorough examination of the temporal spreading diameter variation of droplets on a wedge surface of $\phi_1 = \phi_2 = 45^\circ$ for both 2D and three-dimensional (3D) domains. We observed that the maximum deviation between the results was below 5.25% (refer to [figure 1d](#)). Given the small differences between the 2D and 3D simulation results, we chose 2D simulations (reduced computational expenses), wherever applicable without the loss of relevant mechanics. As and where essential in accordance with the nature of the impact or splitting events, we also performed 3D simulations.

3. Experimental methodology

We performed detailed experiments of the different simulations. A schematic of the experimental set-up is shown in [figure 2a](#). We used a set of carefully machined and surface-polished aluminium wedges with varying dimensions for both symmetric and asymmetric configurations, as illustrated in [figure 2b](#), which were then coated with a commercial superhydrophobic solution (Neverwet, Ultra Ever dry, USA) [38,39]. Before coating, each wedge was cleaned with deionized water, followed by acetone, and oven-dried thoroughly to remove machining oils and debris, dirt and contaminants. The deionized water droplets, with thermophysical properties density (ρ) = 995.67 kg m^{-3} , surface tension (σ) = 71.03 mN m^{-1} and viscosity (η) = 0.791 mPa s at 25°C , were actively dispensed on to the wedge apex using a digitized droplet dispensing mechanism (DDM) (Holmarc Opto-Mechatronics Ltd., India) integrated with a micro-litre syringe ($\pm 0.1 \text{ }\mu\text{l}$ volumetric accuracy) and a flat-head steel needle. The volume of the liquid droplet dispensed was precisely controlled using a digitized controller. To vary the impact Weber number (We), the droplets were released from different heights using a motorized x–y–z stage attached to the DDM. All hydrodynamic events were recorded (as illustrated in [figure 2a](#)) using a high-speed camera (Fastcam Mini-100, Photron, UK) equipped with a 105 mm focal length macro lens. Recordings were conducted in shadowgraph mode at 4000 frames per second with a resolution of 1024×1024 pixels, a spatial resolution of $8.47 \text{ }\mu\text{m}$ per pixel and shutter speed of $2.7 \text{ }\mu\text{s}$. After recording, droplet spreading diameters on the wedge surface were analysed using ImageJ software.

4. Results and discussions

(a) Role of wedge angle (ϕ) on spreading dynamics for symmetric wedges

First, we examine the case of symmetric wedges, exploring various wedge angles, ranging from $\phi = 45^\circ$ to 75° , while maintaining a fixed We (approx. 9.25). We define the contact diameter as the length on the contact line on the wedge surface and trace its variation over time. [Figure 3a–c](#) illustrates the effect of ϕ on the temporal evolution of the droplet spreading, starting from the apex of the wedge. The spread factor ($\beta = D/D_0$) is defined as a ratio of spreading diameter (D) at any instant to pre-impact droplet (D_0). From [figure 3a,b](#), it is evident that β decreases as ϕ increases. This is due to the sharper inclination of the wedge, which limits the available contact area, resulting in less spreading across the surface. Our simulations are supported by experimental results (see [figure 3c](#)), demonstrating a significant relationship between β and the non-dimensional time ($\tau = tU_0/D_0$), where t , U_0 and D_0 represents the elapsed time, impact velocity and pre-impact droplet diameter, respectively. An average deviation of only approximately 8% is noted between the experiments and 2D simulations in [figure 3](#). It is

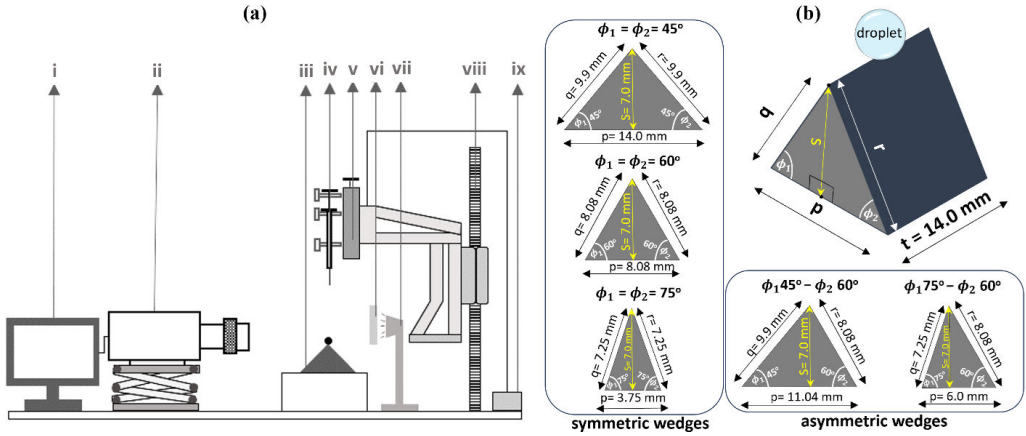


Figure 2. (a). Schematic of the experimental set-up: (i) computer system for camera control and data acquisition, (ii) high-speed camera, (iii) superhydrophobic wedge target, (iv) micro-litre syringe, (v) DDM unit, (vi) diffuser, (vii) strobe light, (viii) motorized x–y–z stage, (ix) DDM controller (b). Wedge dimensions for both symmetric and asymmetric configurations.

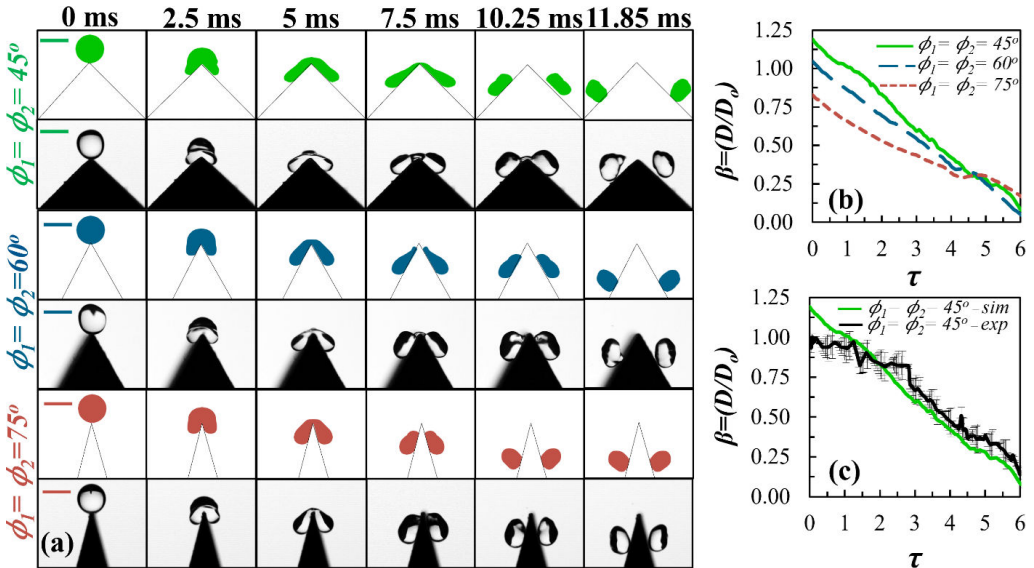


Figure 3. Effect of the wedge angle (ϕ) on the spreading dynamics: (a) Temporal evolutions of the droplet for a fixed We (approx. 9.25) (each odd and even row represents simulation and corresponding experimental observations, respectively), (b) variation in β for different ϕ from simulation, (c) experimental comparison of the β for $\phi_1 = \phi_2 = 45^\circ$. The scale bars in (a) represent 2.8 mm.

important to note that the splitting of the droplet at the wedge apex is accurately predicted by the simulations. However, during lift-off from the wedge sides (see 6th column of figure 3a), we observe that droplet lift-off occurs faster than predicted by the simulations, regardless of ϕ . This discrepancy may arise from the 2D nature of the simulations.

(b) Role of We on maximum spread factor $(\beta)_{\max}$ of the droplet for symmetric wedges

Next, for the symmetric wedges, we examine the effect of We on the maximum spread factor $(\beta)_{\max}$ defined as the ratio of maximum spreading diameter (D_{\max}) at any instant to pre-impact droplet (D_0). As observed from figure 4a,b, it is evident that at a particular ϕ , $(\beta)_{\max}$ increases

with an increase in We , owing to the higher inertial forces during impact. It is also clear that $(\beta)_{\max}$ decreases with an increase in ϕ at a particular We , owing to the sharp steepness of the wedge, which provides less contact area for the droplet to spread out. We verified the simulation results with our experiments and found close agreement, particularly for a wedge with $\phi_1 = \phi_2 = 60^\circ$, where the maximum deviation across various We values is approximately 22.8%. To ensure the validity of this observation, we conducted additional 3D simulations, which confirmed a deviation of approximately 13.63%, further validating the experimental findings.

(c) Role of wedge asymmetry ($\phi_1 - \phi_2$) on the spreading dynamics for asymmetric wedges

Next, we examine the role of wedge asymmetry ($\phi_1 45^\circ - \phi_2 60^\circ$) on spreading dynamics at a fixed We (approx. 9.25). As shown in figure 5a,b, on asymmetric wedges, β increases relatively more along the less steep side ($\phi_1 = 45^\circ$) than on the steeper side ($\phi_2 = 60^\circ$). This is because one side ($\phi_1 = 45^\circ$) of the wedge allows spreading more easily owing to a larger contact area compared with the other side ($\phi_2 = 60^\circ$). The observations are similar on the ($\phi_1 75^\circ - \phi_2 60^\circ$) asymmetric wedge. We further verify the behaviour of β with τ for the asymmetric wedge ($\phi_1 45^\circ - \phi_2 60^\circ$) through experiments (see figure 5c). The experimental results show good agreement with the simulations, with a maximum deviation of approximately 27.9%. This significant deviation is observed only in this specific case among all the cases discussed in §4a–d. To ensure the validity of this observation, we conducted additional 3D simulations, which confirmed a deviation of approximately 11%, further validating the experimental findings. It is also important to mention here that while the splitting event of the droplet is accurately predicted by the 2D simulations, the lift-off after the split is not captured accurately (see last column, figure 5a). This is especially true for the strongly asymmetric wedge ($\phi_1 75^\circ - \phi_2 60^\circ$). This discrepancy can be attributed primarily to the 2D nature of the simulations, where contact-line dynamics and the dynamic contact-angle behaviour along the third coordinate are absent. One potential reason for the mismatch in the lift-off event for asymmetric wedges (last column, figure 5a) may be the non-uniformity of the superhydrophobic coating on the wedge surface [40]. Another reason could be the machining imperfections on the wedge's slant surfaces, which may lead to uneven splitting owing to variations in surface roughness. Even on perfectly symmetric wedges, small air movements during the droplet's free fall might make the droplet hit the wedge slightly off-centre, adding to the asymmetry. Together, these factors: 2D simulation limits, uneven superhydrophobic coating, surface roughness and air effects, account for the differences observed in lift-off between experiments and simulations. To investigate these possible explanations in more detail, we extended our analysis through impact-force tracing (§4i).

(d) Role of We on $(\beta)_{\max}$ for asymmetric wedges

Continuing from our previous discussion (§4c) of wedge asymmetry and its influence on droplet spreading dynamics, we now focus on the effect of We on $(\beta)_{\max}$. As shown in figure 6a,b, $(\beta)_{\max}$ increases with an increase in We owing to the higher inertial forces available during impact at the apex. In addition, similar to the findings in the asymmetric wedges ($\phi_1 45^\circ - \phi_2 60^\circ$), the less steep side of the wedge results in a relatively larger $(\beta)_{\max}$ compared with the steeper side. This is because the gentler slope provides a larger available contact area, allowing the droplet to spread more easily. The same trend is observed in the wedge with angles ($\phi_1 75^\circ - \phi_2 60^\circ$). A comparison between our simulation results and experimental data shows a deviation of approximately 9%.

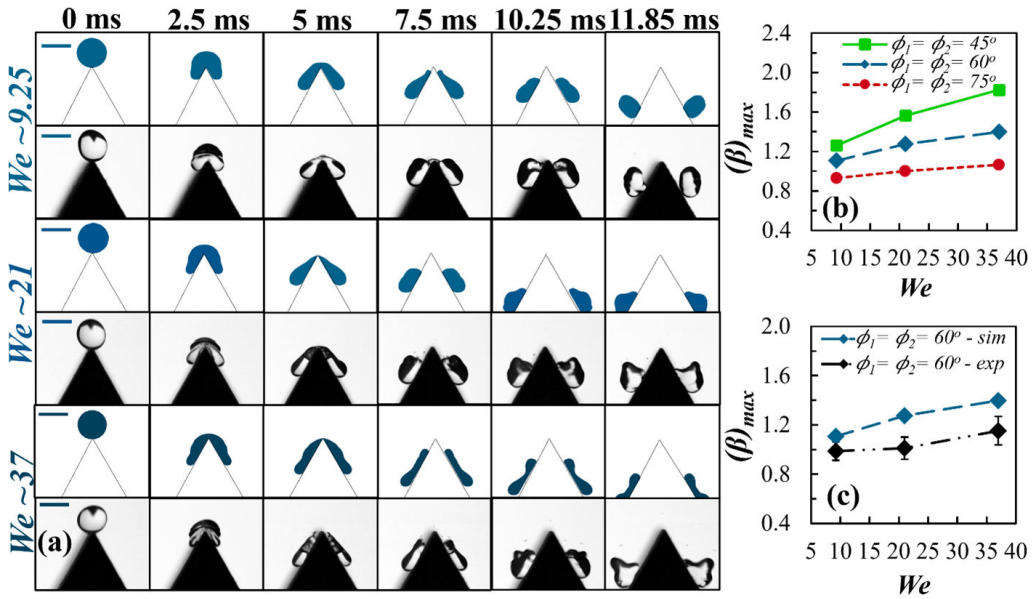


Figure 4. Effect of Weber number (We) on the spreading dynamics: (a) temporal evolutions of the droplet for $\phi_1 = \phi_2 = 60^\circ$ (each odd and even row represents simulation and corresponding experimental observations, respectively), (b) variation in $(\beta)_{\max}$ for different ϕ from simulations, (c) experimental comparison of the $(\beta)_{\max}$ for $\phi_1 = \phi_2 = 60^\circ$. The scale bars in (a) represent 2.8 mm.

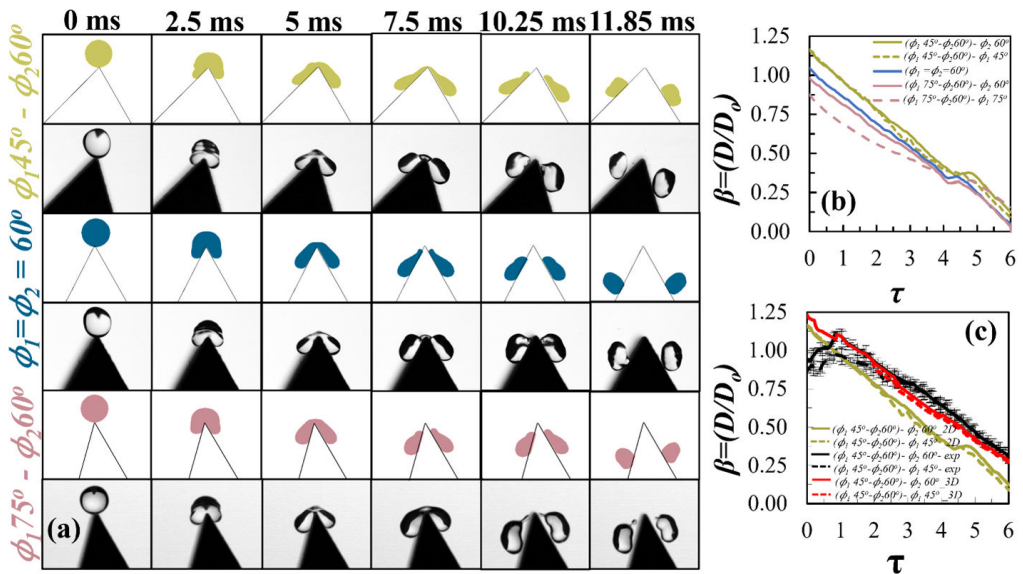


Figure 5. Influence of the wedge asymmetry angle ($\phi_1 - \phi_2$) on the spreading dynamics: (a) temporal evolutions for a fixed We (approx. 9.25) (each odd and even row represents simulation and corresponding experimental observations, respectively), (b) variation in β for different $(\phi_1 - \phi_2)$, (c) experimental comparison of β with 2D and 3D plot trends for $(\phi_1 45^\circ - \phi_2 60^\circ)$. The scale bars in (a) represent 2.8 mm.

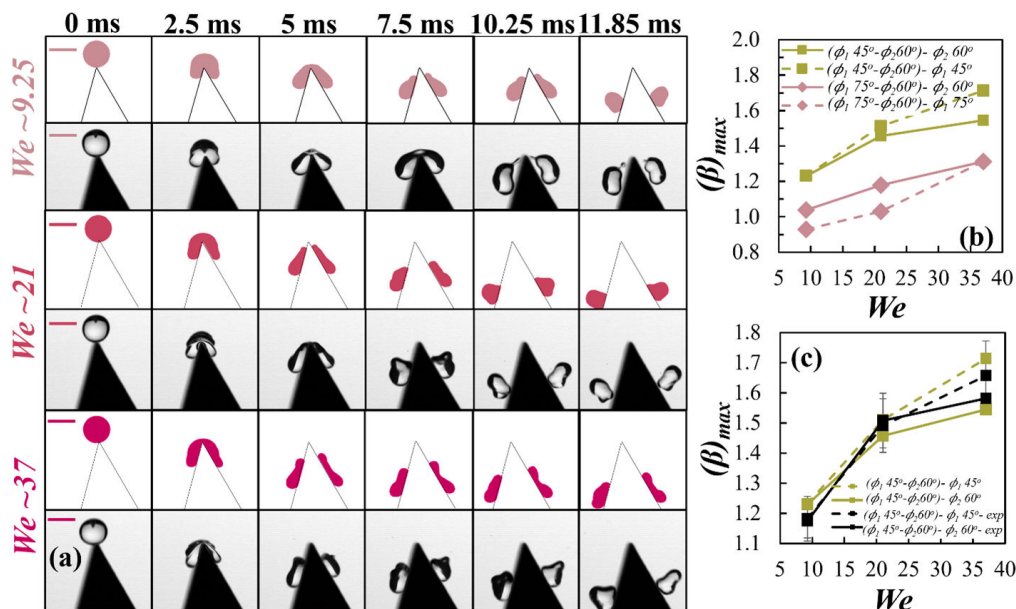


Figure 6. Influence of the We on the spreading dynamics: (a) Temporal evolutions of the droplet for $(\phi_1 75^\circ - \phi_2 60^\circ)$ (each odd and even row represents simulation and corresponding experimental observations, respectively), (b) maximum spread factor $(\beta)_{\max}$ for different wedge angles, (c) experimental comparison of the $(\beta)_{\max}$ for $(\phi_1 45^\circ - \phi_2 60^\circ)$. The scale bars in (a) represent 2.8 mm.

(e) Role of normalized bond number (Bo^*) on the spreading dynamics for symmetric wedges

To examine whether droplet size affects the splitting behaviour during impact on a superhydrophobic wedge, we extended our investigation to analyse both the spreading and splitting behaviours of droplets with different size. The droplet size indirectly affects the characteristic length scale, known as the capillary length (λ) ($= (\sqrt{\sigma/\rho g}$, where σ is the surface tension, ρ is the density and g is the acceleration owing to gravity), which represents the balance between gravitational and surface tension forces. For a water droplet at 25°C , this length scale is approximately 2.8 mm. To capture this interplay for droplets of varying sizes 2.04–3.5 mm, we introduce a normalized Bond number (Bo^*) as the ratio of the operating Bond number (Bo) to the Bond number for the capillary length scale ($Bo_{\text{capillary}} = \rho g D_o^2 / \sigma$ with $= 2.8$ mm for all cases). The operating Bond number (Bo) is a dimensionless quantity that represents the ratio of gravitational force to surface tension force, expressed as ($Bo = \rho g D_o^2 / \sigma$), where ρ is the density, g is the acceleration owing to gravity, D_o is the pre-impact droplet diameter and σ is the surface tension.

We now discuss the effect of Bo^* on the spreading dynamics of droplets impacting symmetric wedges. The variation of D_o between 2.04 and 3.5 mm was used to adjust Bo . Figure 7a shows the temporal evolution of a droplet on a symmetric wedge ($\phi_1 = \phi_2 = 45^\circ$) for different values of Bo^* . We observe that droplets with higher Bo^* (i.e. $Bo^* = 1.5$) lift-off the wedge surface more quickly than those with low Bo^* (i.e. $Bo^* = 0.5$), which can be attributed to the dominance of gravitational forces over capillary forces. Although this may seem counterintuitive, as stronger gravitational forces are expected to cause more spreading, larger Bo^* droplets exhibit earlier lift-off with intermediate liquid-bridge formation (refer to 6th row, 5th column of figure 7a). This phenomenon could result from the inertial collapse of the droplet at the onset of splitting, leading to immediate lift-off.

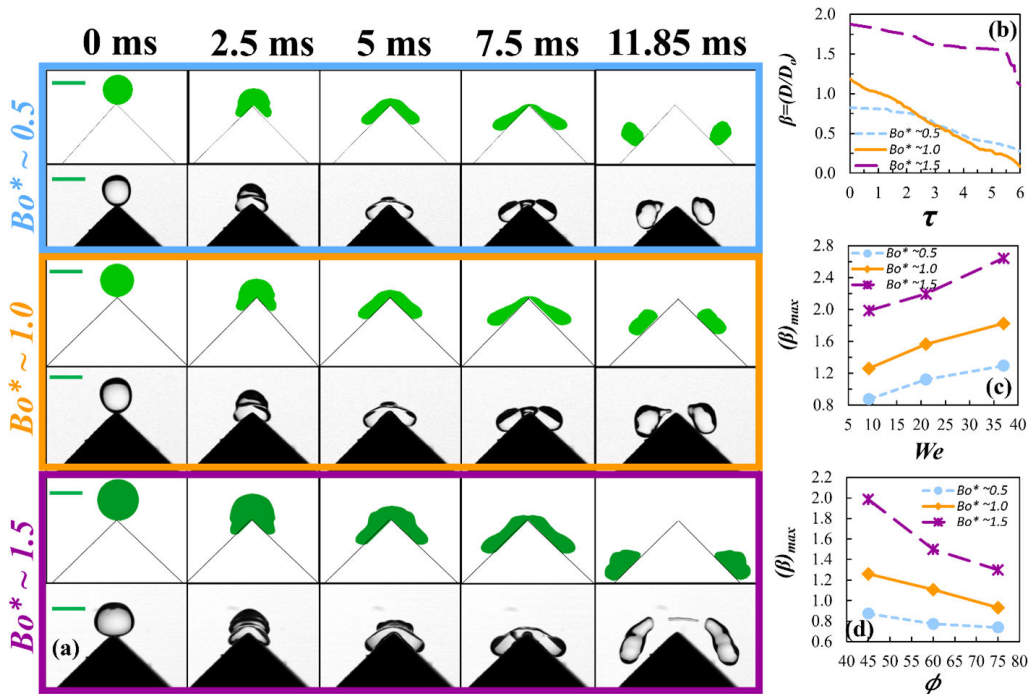


Figure 7. Effect of the Bo^* on the spreading dynamics at a fixed We (approx. 9.25) for $(\phi_1 = \phi_2 = 45^\circ)$: (a) snapshots of the time evolutions of droplet over different Bo^* (each odd and even row represents simulation and corresponding experimental observations respectively), (b) variation in β under varying Bo^* , (c) change in $(\beta)_{\max}$ over different Bo^* against various We , (d) variation in $(\beta)_{\max}$ for different ϕ . The scale bars in (a) represent 2.8 mm.

Figure 7b illustrates that β decreases with increasing τ for a fixed Bo^* , and the trend shifts upward with larger D_0 . In figure 7c, we notice that $(\beta)_{\max}$ increases with Bo^* at a given We owing to the greater influence of gravitational forces. Similarly, $(\beta)_{\max}$ increases with We at a fixed Bo^* owing to higher inertial forces. Figure 7d shows that $(\beta)_{\max}$ decreases with increasing ϕ for a given Bo^* and We , owing to the wedge's steepness, which reduces the contact area for spreading. Furthermore, it is also evident that at fixed ϕ and We , $(\beta)_{\max}$ increases with Bo^* owing to the stronger dominance of gravitational forces over capillary forces.

(f) Role of Bo^* on the spreading dynamics for asymmetric wedges

Expanding on the earlier discussion, we now examine the influence of wedge asymmetry on the spreading and splitting behaviours of droplets for varying Bo^* . Figure 8a presents the temporal evolutions of the droplet on an asymmetric wedge ($\phi_1 75^\circ - \phi_2 60^\circ$). From figure 8b, it is evident that the trend of β over τ shifts upward with an increase in Bo^* at a particular We (approx. 9.25). This is due to the dominance of gravitational forces against capillary forces. In addition, for a fixed Bo^* and We , the less steep side ($\phi_2 = 60^\circ$) of the wedge allows for easier droplet spreading owing to greater contact area compared with the steeper side ($\phi_1 = 75^\circ$). Similarly, figure 8c shows the change in $(\beta)_{\max}$ across different Bo^* at varying We . We observe that $(\beta)_{\max}$ increases with Bo^* at a fixed We owing to the dominant gravitational forces over capillary forces. Further, it is also noticed that at the same Bo^* , $(\beta)_{\max}$ increases with an increase in We owing to greater influence of inertial forces over capillary forces. Among all operated cases, the less steep side and large Bo^* at higher We exhibit larger $(\beta)_{\max}$ of the droplet owing to the stronger dominance of both inertial and gravitational forces over the capillary forces.

By contrast to the symmetric case ($\phi_1 = \phi_2 = 45^\circ$), the asymmetric case ($\phi_1 75^\circ - \phi_2 60^\circ$) shows earlier droplet lift-off at low Bo^* and fixed We . This is a result of the strong influence of wedge

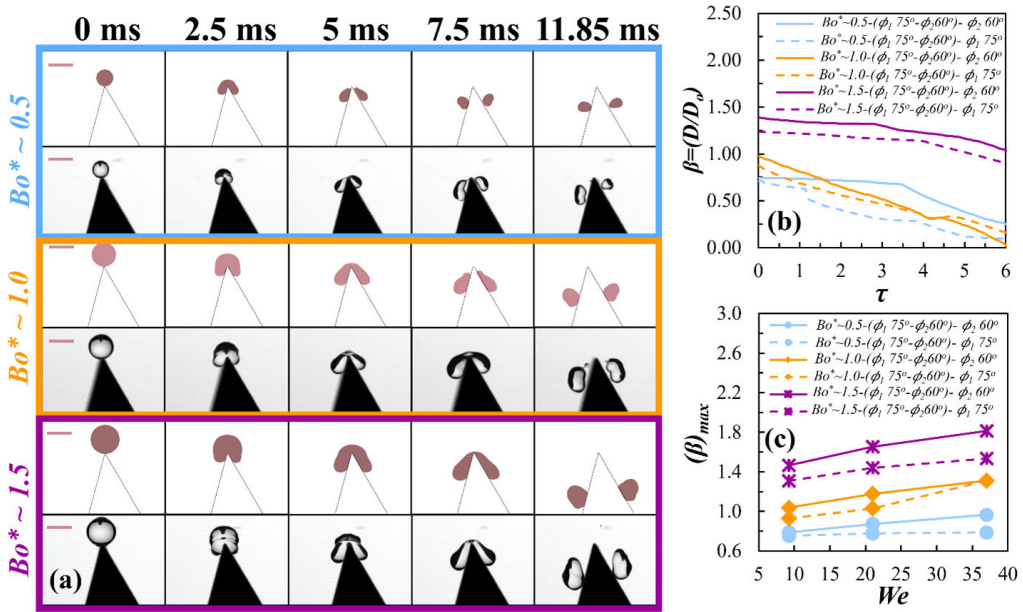


Figure 8. Effect of Bo^* on the spreading dynamics for $(\phi_1 75^\circ - \phi_2 60^\circ)$ asymmetric wedge: (a) temporal evolutions of droplet for different Bo^* (each odd and even rows represent simulation and corresponding experimental observations, respectively), (b) β over varying Bo^* at a fixed We (approx. 9.25), (c) change in $(\beta)_{max}$ for different Bo^* against various We . The scale bars in (a) represent 2.8 mm.

asymmetry. Since both sides of the asymmetric wedge have unequal spreading areas and lift-off time scales, both sides hinder immediate lift-off during the split-up phase, thus suppressing post-split lift-off.

(g) Role of wedge asymmetry on the non-dimensional split volume (V^*) of the droplet

In §4a–f we explored the spreading dynamics and splitting behaviour of droplets. Now, we shift our attention to focus on the split volumes of the daughter droplets during the post-split phase. Through 3D numerical simulations, the variation in the non-dimensional split volume ($V^* = V_{daughter} / V_{parent}$) of daughter droplets during the split-up phase over different ϕ are shown in figure 9a. The results show that the V^* increases as ϕ increases from 45° to 75° at a fixed We (approx. 9.25), owing to the steeper wedge promoting more significant droplet splitting. Similarly, we show the variation in V^* during the split-up phase on asymmetric wedges $(\phi_1 - \phi_2)$ at the same We (approx. 9.25) in figure 9b. It is observed that the gentler side ($\phi_1 45^\circ$) of $(\phi_1 45^\circ - \phi_2 60^\circ)$ wedge generates a smaller V^* compared with the steeper side ($\phi_1 75^\circ$) of $(\phi_1 75^\circ - \phi_2 60^\circ)$ wedge. Here, it has been noted that the less steep side $\phi_1 = 45^\circ$ (refer to blue colour bar in figure 9b) of $(\phi_1 45^\circ - \phi_2 60^\circ)$ wedge generates a smaller V^* than the steeper side $\phi_2 = 60^\circ$ of the same asymmetric wedge. Similarly, $(\phi_1 75^\circ - \phi_2 60^\circ)$ wedge generates more V^* on the steeper side ($\phi_1 = 75^\circ$) (refer to red colour bar in figure 9b) than the gentler side ($\phi_2 = 60^\circ$) owing to less spreading area available for the droplet to spread out against the splitting event. Since we dealt with a lower We , both 3D numerical simulations and experimental observations show that fragmentation during split-up phase is insignificant compared with the formation of main daughter droplets.

(h) Energy budget of the post-impact droplet on symmetric wedges

In §4a–f, we observed a certain degree of deviation (approx. 5–14%) between the 2D simulation results and our experimental observations. Notably, the 2D model was unable to accurately

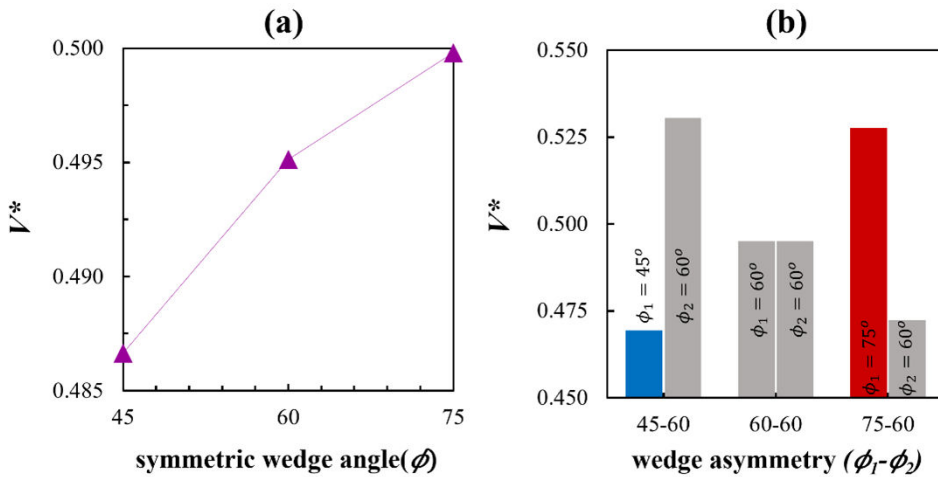


Figure 9. Numerical 3D simulation results of variation in non-dimensional split volume (V^*) of daughter droplets during split-stage of the parent droplet (a) for different ϕ (b) for different $(\phi_1 - \phi_2)$.

predict the late-stage or splitting hydrodynamics of the droplets. To address this, we now extend our analysis to 3D simulations, aiming to better understand the energy budget of the post-impact droplets and determine whether these simulations can more accurately track the splitting behaviour. Unlike the behaviour observed on solid-horizontal and solid-inclined superhydrophobic surfaces [20,41], we noticed that droplets on the slanted superhydrophobic wedge not only split but also slide along the wedge edges, accompanied by retraction and lift-off events. In this section, we analyse the droplet shape deformation and energy conversion throughout the entire cycle, from pre-impact to the lift-off of the daughter droplets from the wedge surface. Comparing our findings with those of [20], where the total energy at a normal We of 37 is approximately $7.5 \mu\text{J}$, our study at a lower We (approx. 9.25) shows a significantly smaller total energy of approximately $5 \mu\text{J}$. This highlights the distinct energy dynamics influenced by the parametric conditions and the wedge geometry.

The three relevant energy components for droplet impact are as follows: kinetic energy (E_K^o), potential energy (E_P^o) and surface energy (E_S^o). The total initial energy of the droplet just prior to impact is $E_0 = E_K^o + E_P^o + E_S^o$. Energy conservation at time t post-impact yields

$$E_0 = E_P^{(t)} + E_K^{(t)} + E_D^{(t)} + E_S^{(t)}, \quad (4.1)$$

where E_0 , $E_P^{(t)}$, $E_K^{(t)}$, $E_D^{(t)}$, $E_S^{(t)}$ represent the total initial energy, potential energy, kinetic energy, viscous dissipation energy and surface energy at time t , respectively. Further, to account for energy loss to the surrounding air, kinetic energies are separately considered for the droplet $E_{K,d}^{(t)}$, and ambient gas (air) $E_{K,g}^{(t)}$. The energy components are determined by evaluating integrals from the numerical simulations as

$$E_{K,d}^{(t)} = \frac{1}{2} \int_{V_d} \rho_d |V|^2 dV_d, \quad (4.2)$$

$$E_{K,g}^{(t)} = \frac{1}{2} \int_{V_g} \rho_g |V|^2 dV_g, \quad (4.3)$$

$$E_P^{(t)} = \rho_d g \int_{V_d} h_c dV_d. \quad (4.4)$$

The viscous dissipation within the droplet is obtained using equations (4.5)–(4.7), as

$$E_D^{(t)} = \int_0^t W(t) dt. \quad (4.5)$$

Here, the viscous dissipation rate $W(t)$ is evaluated in terms of the stress tensor and the rate of the stress tensor \mathbf{S} , as

$$W(t) = \int_{V_dUV_g} \mathbf{T} : \mathbf{S} dV, \quad (4.6)$$

$$W(t) = \int_{V_dUV_g} \left[2\mu \left[\left(\frac{\partial V_x}{\partial x} \right)^2 + \left(\frac{\partial V_y}{\partial y} \right)^2 + \left(\frac{\partial V_z}{\partial z} \right)^2 - \frac{1}{3} (\nabla \cdot \mathbf{V})^2 \right] + \mu \left[\left(\frac{\partial V_y}{\partial x} + \frac{\partial V_x}{\partial y} \right)^2 + \left(\frac{\partial V_z}{\partial y} + \frac{\partial V_y}{\partial z} \right)^2 + \left(\frac{\partial V_x}{\partial z} + \frac{\partial V_z}{\partial x} \right)^2 \right] \right] dV. \quad (4.7)$$

The surface energy of the droplet is calculated from

$$E_S(t) = \int_A \gamma dA, \quad (4.8)$$

where A represents the surface area of the droplet.

In this context, it is noticed that when a droplet impacts the apex of a ($\phi_1 = \phi_2 = 45^\circ$) wedge with fixed We (approx. 9.25) (refer to figure 10a), it spreads along the slant edge without splitting for 5 ms (refer to 3rd column of figure 10a–d). At approximately 7.5 ms, it splits into two nearly equal daughter droplets, which spread and slide along the edge, lifting-off at approximately 11.85 ms (refer to 5th column of figure 10a–d). After the drop impact on the wedge, the kinetic energy of the droplet decreases while the surface energy increases during spreading. Post-split, the daughter droplets continue spreading and eventually reach maximum surface energy at maximum spread state. Subsequently, the daughter droplets retract with increased kinetic energy until lift-off. During the lift-off, the viscous dissipation energy rises as the droplets become ellipsoidal (refer to figure 10d and red diamond trend line in figure 10e). As shown in figure 10f, increase of the wedge angle from $\phi = 45^\circ$ to $\phi = 75^\circ$ reduces the split time from approximately 6.25 ms to approximately 5 ms owing to the variation in the steepness. Velocity profiles (refer to figure 10f) show that higher ϕ cause the droplet to split and roll post-impact, owing to reduced spread area. Figure 10g shows pressure peaks during pre-impact and split-up stages, caused by sudden changes in three-phase contact-line velocities and high capillary wave oscillations [42] at the liquid–air interface during spreading. We believe that the significant changes in velocity contours and pressure distribution are due to the triple contact line on the wedge surface acting as a moving wave source [42], generating local curvature gradients. This causes capillary wave oscillations at the onset of split-up, leading daughter droplets to roll instead of slide (refer to 4th and 5th columns of figure 10f).

(i) Impact-force history

Finally, through numerical simulations, we investigated the impact-force $F(t)$ history of a 3D droplet on both symmetric ($\phi_1 = \phi_2 = 45^\circ$) and asymmetric ($\phi_1 45^\circ - \phi_2 60^\circ$) superhydrophobic wedge surfaces at fixed We (approx. 9.25) (refer to figure 11). The impact force exerted by the droplet on the surface is obtained by integrating the pressure field on the wedge as shown in equation (4.9).

$$F(t) = \int_A (p) dA. \quad (4.9)$$

On one hand, when a droplet impacts on the apex portion ($t \sim 0$ ms) of the symmetric ($\phi_1 = \phi_2 = 45^\circ$) superhydrophobic wedge, there is a sudden rise in its impact force and reaches a maximum value of $F_{1(\phi_1 = 45^\circ)} = F_{1(\phi_2 = 45^\circ)} = 0.0045 \mu\text{N}$ (refer to state B in figure 11) during the onset of the spreading stage ($t \sim 2.6$ ms). After that, the parent droplet starts to spread and reaches a minimum value of $0.0038 \mu\text{N}$ at the maximum spreading stage without split ($t \sim 5$ ms). The force continues to decrease to $0.00286 \mu\text{N}$ as the parent droplet splits into two nearly equal daughter droplets ($t \sim 7.25$ ms). Once the droplet splits up into two daughter droplets, they separately retract against sliding on the two slant sides of the symmetric superhydrophobic

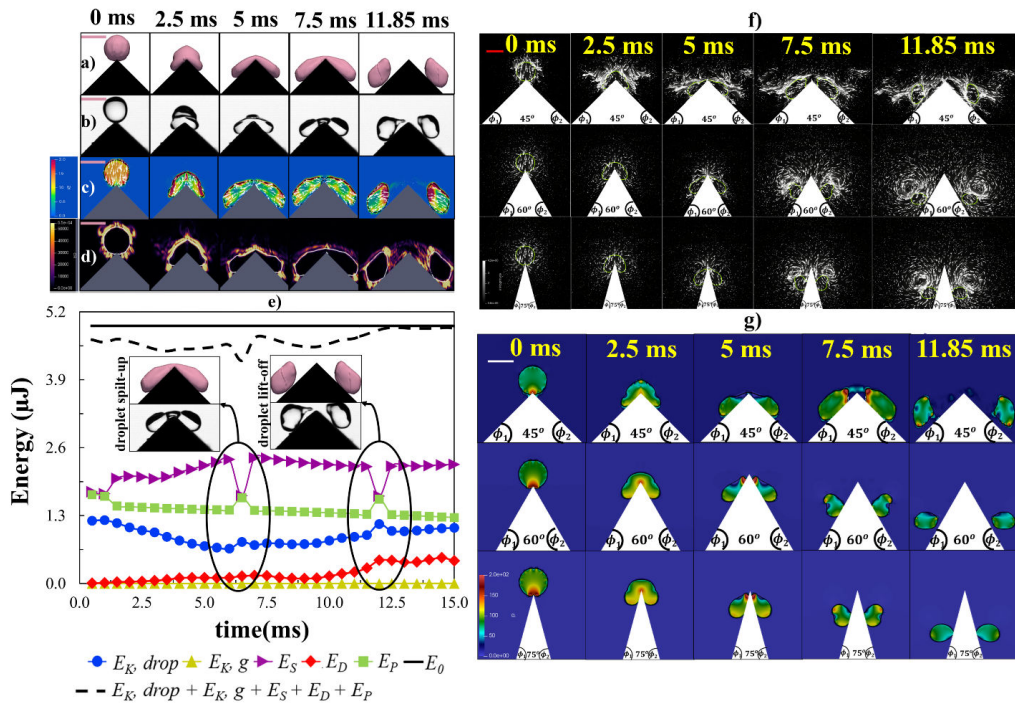


Figure 10. Temporal evolutions of the 3D droplet for $(\phi_1 = \phi_2 = 45^\circ)$ at a fixed We (approx. 9.25). (a) 3D simulation, (b) experimental, (c) kinetic energy distribution across the droplet per unit volume ($\mu\text{J m}^{-3}$), (d) viscous dissipation energy distribution across the droplet per unit volume per unit time ($\mu\text{J m}^{-3} \text{s}$) and (e) energy-budget estimation. (f) Velocity distribution, (g) pressure variation. The scale bars in (a–g) represent 2.8 mm.

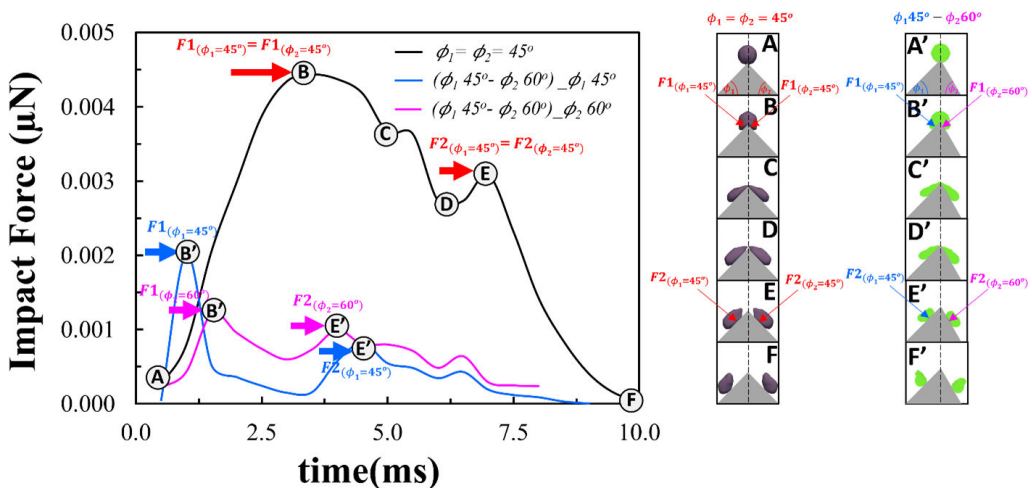


Figure 11. Impact-force history of the 3D droplet on $(\phi_1 = \phi_2 = 45^\circ)$ and $(\phi_1 45^\circ - \phi_2 60^\circ)$ superhydrophobic wedge surfaces at fixed We (approx. 9.25).

wedge. Owing to the large amount of local viscous dissipation and capillary-wave [42] generation at the interface of the droplet, its shape becomes transformed from spheroidal to ellipsoid. At this instance, we note that there is a gradual secondary peak in the impact force (refer to state E in figure 11) of $F2_{(\phi_1 = 45^\circ)} = F2_{(\phi_2 = 45^\circ)} = 0.00318 \mu\text{N}$ during the onset of retraction stages of the two daughter droplets against sliding at $t \sim 8.5$ ms owing to the stored impact kinetic energy. Subsequently, following this secondary peak (refer to state E in figure 11),

the impact force steadily decreases until it reaches zero as the two daughter droplets lift-off ($t \sim 10.75$ ms) the wedge sides. Unlike earlier reports [20,43], which report two main peaks in the impact force, one during initial spreading and another at maximum spreading, along with a detailed analysis of velocity and dissipation, our study highlights a secondary peak in the impact force during the retraction of the daughter droplets after splitting. This finding emphasizes the role of viscous dissipation and capillary waves in the evolution of the impact force.

On the other hand, when the same droplet impacts the apex portion ($t \sim 0$ ms) of an asymmetric superhydrophobic wedge ($\phi_1 45^\circ - \phi_2 60^\circ$), similar to the symmetric ($\phi_1 = \phi_2 = 45^\circ$) case, initially there is a sudden rise in its impact force, reaching a peak $F_{1(\phi_1 = 45^\circ)} = 0.0021 \mu\text{N}$ and $F_{1(\phi_2 = 60^\circ)} = 0.00145 \mu\text{N}$ on the less steeper ($\phi_1 = 45^\circ$) and steeper ($\phi_2 = 60^\circ$) sides, respectively (refer to B' on both blue and pink colour trend lines in figure 11). This is due to the change in unequal available spreading areas, which creates strong competition between spreading and splitting. Consequently, there is a mismatch in the time intervals for the droplet to split on both sides of the wedge. Similarly, post split-up, the retraction and lift-off time scales of daughter droplets are also different owing to the unequal volumes of the daughter droplet generation in the asymmetric wedge case. This led to an abrupt change in the secondary peak in impact force $F_{2(\phi_1 = 45^\circ)} = 0.00085 \mu\text{N}$ and $F_{2(\phi_2 = 60^\circ)} = 0.00105 \mu\text{N}$ on the gentler ($\phi_2 = 45^\circ$) and steeper ($\phi_2 = 60^\circ$) sides, respectively (refer to E' on both blue and pink colour trend lines in figure 11).

5. Conclusions

In conclusion, for symmetric superhydrophobic wedges, we found that water droplets spread more easily as ϕ decreases rather than rolling, even with nearly equal volumes of the daughter droplets at a fixed We . Droplets exhibit larger spreading with an increase in We for a fixed wedge angle (ϕ) owing to the dominant inertial forces than capillary forces. We also show that $(\beta)_{\max}$ decreases with an increase in ϕ at a fixed We owing to the greater steepness, which reduces the available contact area for droplet spreading. For asymmetric wedges ($\phi_1 - \phi_2$), we found that the spread factor (β) increases relatively more on the gentler side than the steeper side. Post split, the parent droplet generates unequal volumes of daughter droplets under varying We . It is revealed that, among all operated cases, ($\phi_1 75^\circ - \phi_2 60^\circ$) splits a larger volume of the daughter droplets on the steeper side ($\phi_1 = 75^\circ$) owing to less spread area of the droplet to spread out against splitting.

For both symmetric and asymmetric cases, $(\beta)_{\max}$ of the droplet increases with an increase in Bo^* owing to a larger D_o regardless of any particular We . By estimating the energy budget for the complete lift-off cycle of an impacting water droplet on a symmetric superhydrophobic wedge, we found a strong competition between surface energy and stored kinetic energy during the retraction phase. This interplay significantly influences the rise in viscous dissipation during the split-up to lift-off stages (refer to the 4th–6th columns of figure 10c,d). Our numerical evaluation of the impact-force history (refer to figure 11) shows substantial fluctuations with peaks during the onset of droplet spreading and daughter droplet retraction phases on both symmetric and asymmetric superhydrophobic wedges. Our findings provide valuable insights into droplet splitting against stationary or moving obstacles in micro- and macro-fluidic scenarios. This investigation could be instrumental in designing systems for applications involving controlled droplet manipulation [44,45].

Data accessibility. All data pertaining to this research work are available in the manuscript. Code for the open-source solver OpenFOAM is available from the Zenodo repository [46].

Data also available from the GitHub Repository [47].

Declaration of AI use. We have not used AI-assisted technologies in creating this article.

Authors' contributions. G.V.V.S.V.P.: conceptualization, data curation, formal analysis, investigation, methodology, software, writing—original draft; P.K.: conceptualization, formal analysis, funding acquisition, project administration, resources, software, supervision, writing—original draft; P.D.: conceptualization, investigation, methodology, project administration, supervision, writing—original draft, writing—review and editing; D.S.: conceptualization, funding acquisition, investigation, project administration, resources, supervision, writing—original draft.

All authors gave final approval for publication and agreed to be held accountable for the work performed therein.

Conflict of interest declaration. We declare we have no competing interests.

Funding. All authors would like to acknowledge National Supercomputing Mission (NSM) for providing computing resources of PARAM Himalaya at IIT Mandi, which is implemented by C-DAC and supported by the Ministry of Electronics and Information Technology (MeitY) and Department of Science and Technology (DST), Government of India.

Acknowledgements. G.V.V.S.V.P. would like to thank the Ministry of Education, Govt. of India, for the doctoral scholarship. G.V.V.S.V.P. would like to thank Debarshi Debnath for his helpful support and fruitful discussions for the present work. P.K. would like to thank IIT Mandi for providing computational resources for the present work.

References

1. Josserand C, Thoroddsen S, Josserand C, T. S, Annual S, Mechanics F. 2017 Drop impact on a solid surface to cite this version: HAL Id: hal-01398138 drop impact on a solid. *Annu. Rev. Fluid Mech.* **48**, 365–391. (doi:10.1146/annurev-fluid-122414-034401)
2. Yarin AL. 2006 Drop impact dynamics: splashing, spreading, receding, bouncing.... *Annu. Rev. Fluid Mech.* **38**, 159–192. (doi:10.1146/annurev.fluid.38.050304.092144)
3. Biance AL, Clanet C, Quéré D. 2004 First steps in the spreading of a liquid droplet. *Phys. Rev. E* **69**, 4. (doi:10.1103/PhysRevE.69.016301)
4. Antonini C, Villa F, Bernagozzi I, Amirfazli A, Marengo M. 2013 Drop rebound after impact: the role of the receding contact angle. *Langmuir* **29**, 16045–16050. (doi:10.1021/la4012372)
5. Howland CJ, Antkowiak A, Castrejón-Pita JR, Howison SD, Oliver JM, Style RW, Castrejón-Pita AA. 2016 It's harder to splash on soft solids. *Phys. Rev. Lett.* **117**, 1–5. (doi:10.1103/PhysRevLett.117.184502)
6. Laan N, de Bruin KG, Bartolo D, Josserand C, Bonn D. 2014 Maximum diameter of impacting liquid droplets. *Phys. Rev. Appl.* **2**, 1–7. (doi:10.1103/PhysRevApplied.2.044018)
7. Andrade R, Skurtys O, Osorio F. 2013 Drop impact behavior on food using spray coating: fundamentals and applications. *Food Res. Int.* **54**, 397–405. (doi:10.1016/j.foodres.2013.07.042)
8. Leidenfrost JG. 1756 De aquae communis nonnullis qualitatibus tractatus. Ovenius.
9. Prasad GVV, Dhar P, Samanta D. 2022 Postponement of dynamic Leidenfrost phenomenon during droplet impact of surfactant solutions. *Int. J. Heat Mass Transf.* **189**, 122675. (doi:10.1016/j.ijheatmasstransfer.2022.122675)
10. V V S Vara Prasad G, Yadav M, Dhar P, Samanta D. 2023 Morphed inception of dynamic Leidenfrost regime in colloidal dispersion droplets. *Phys. Fluids* **35**. (doi:10.1063/5.0131609)
11. Vara Prasad GVVS, Sharma H, Nirmalkar N, Dhar P, Samanta D. 2022 Augmenting the Leidenfrost temperature of droplets via nanobubble dispersion. *Langmuir* **38**, 15925–15936. (doi:10.1021/acs.langmuir.2c01891)
12. He H, Guo Z. 2021 Superhydrophobic materials used for anti-icing theory, application, and development. *iScience* **24**, 103357. (doi:10.1016/j.isci.2021.103357)
13. Hirt CW, Nichols BD. 1981 Volume of fluid (VOF) method for the dynamics of free boundaries. *J. Comput. Phys.* **39**, 201–225. (doi:10.1016/0021-9991(81)90145-5)
14. Brackbill C, Kothe DB. 1992 Brackbill- a continuum method for modeling. *J. Comput. Phys.* **100**, 335–354. (doi:10.1016/0021-9991(92)90240-Y)
15. Shikhmurzaev YD. 2007 Capillary flows with forming interfaces. In *Capill. flows form. interfaces*, pp. 1–478. (doi:10.1201/9781584887492). See <https://www.taylorfrancis.com/books/9781584887492>.

16. Cox RG. 1986 The dynamics of the spreading of liquids on a solid surface. Part 1. Viscous flow. *J. Fluid Mech.* **168**, 169–194. (doi:10.1017/S0022112086000332)
17. Hu A, Liu D. 2022 3D simulation of micro droplet impact on the structured superhydrophobic surface. *Int. J. Multiph. Flow* **147**, 103887. (doi:10.1016/j.ijmultiphaseflow.2021.103887)
18. Debnath D, Kumar P, Mitra SK. 2021 Toward unveiling the anomalies associated with the spontaneous spreading of droplets. *Langmuir* **37**, 14833–14845. (doi:10.1021/acs.langmuir.1c02622)
19. Debnath D, Misra S, Kumar P, Mitra S. 2023 Understanding under-liquid drop spreading using dynamic contact angle modeling. *Phys. Fluids* **35**. (doi:10.1063/5.0167659)
20. Debnath D, Verma D, Kumar P, Balakrishnan V. 2023 Understanding the impact dynamics of droplets on superhydrophobic surface. *Int. J. Multiph. Flow* **159**, 104344. (doi:10.1016/j.ijmultiphaseflow.2022.104344)
21. Henman NIJ, Smith FT, Tiwari MK. 2023 Computational study of early-time droplet impact dynamics on textured and lubricant-infused surfaces. *Int. J. Multiph. Flow* **161**, 104398. (doi:10.1016/j.ijmultiphaseflow.2023.104398)
22. Vontas K, Andredaki M, Georgoulas A, Nikas KS, Marengo M. 2017 Numerical investigation of droplet impact on smooth surfaces with different wettability characteristics: Implementation of a dynamic contact angle treatment in openfoam. In *28th Conference on Liquid Atomization and Spray System*, Valencia, Spain, pp. 6–8. (doi:10.4995/ILASS2017.2017.5020)
23. Malgarinos I, Nikolopoulos N, Marengo M, Antonini C, Gavaises M. 2014 VOF simulations of the contact angle dynamics during the drop spreading: Standard models and a new wetting force model. *Adv. Colloid Interface Sci.* **212**, 1–20. (doi:10.1016/j.cis.2014.07.004)
24. Zhang J, Borg MK, Reese JM. 2017 Multiscale simulation of dynamic wetting. *Int. J. Heat Mass Transf.* **115**, 886–896. (doi:10.1016/j.ijheatmasstransfer.2017.07.034)
25. Liu X, Zhang X, Min J. 2019 Maximum spreading of droplets impacting spherical surfaces. *Phys. Fluids* **31**. (doi:10.1063/1.5117278)
26. Liu X, Min J, Zhang X. 2020 Dynamic behavior and maximum spreading of droplets impacting concave spheres. *Phys. Fluids* **32**. (doi:10.1063/5.0020110)
27. Ding S, Liu X, Wu X, Zhang X. 2020 Droplet breakup and rebound during impact on small cylindrical superhydrophobic targets. *Phys. Fluids* **32**. (doi:10.1063/5.0024837)
28. Luo J, Chu F, Ni Z, Zhang J, Wen D. 2021 Dynamics of droplet impacting on a cone. *Phys. Fluids* **33**. (doi:10.1063/5.0073049)
29. Wasserfall J, Figueiredo P, Kneer R, Rohlf W, Pischke P. 2017 Coalescence-induced droplet jumping on superhydrophobic surfaces: effects of droplet mismatch. *Phys. Rev. Fluids* **2**, 1–17. (doi:10.1103/PhysRevFluids.2.123601)
30. Russo A, Icardi M, Elsharkawy M, Ceglia D, Asinari P, Megaridis CM. 2020 Numerical simulation of droplet impact on wettability-patterned surfaces. *Phys. Rev. Fluids* **5**, 074002. (doi:10.1103/physrevfluids.5.074002)
31. Wang G, Gao J, Luo KH. 2020 Droplet impacting a superhydrophobic mesh array: effect of liquid properties. *Phys. Rev. Fluids* **5**, 1–19. (doi:10.1103/PhysRevFluids.5.123605)
32. Hao J, Lu J, Lee L, Wu Z, Hu G, Floryan JM. 2019 Droplet splashing on an inclined surface. *Phys. Rev. Lett.* **122**, 054501. (doi:10.1103/physrevlett.122.054501)
33. Zhao H, Han X, Li J, Li W, Huang T, Yu P, Wang L. 2022 Numerical investigation of a droplet impacting obliquely on a horizontal solid surface. *Phys. Rev. Fluids* **7**, 1–21. (doi:10.1103/PhysRevFluids.7.013601)
34. Review PA, Devolder B, Schmitt P, Rauwoens P, Elsaesser B, Troch P. 2015 A review of the implicit motion solver algorithm in OpenFOAM® to simulate a heaving buoy. In *18th Numerical Towing Tank Symposium (NuTTS'15)*, Cortona, Italy. <http://www.numeca.com/en/about-us/news/numeca-sponsoring-18thnumerical-towing-tank-symposium-nutts-15>.
35. Stefan F, Kistler. *Hydrodynamics of wetting*, Google books. Google books. See https://books.google.co.in/books?hl=en&lr=&id=v0dZDwAAQBAJ&oi=fnd&pg=PA311&ots=nGzq0WLj8v&sig=NapJxpmKjZRIN0rOZ8ovSEGpZoY&redir_esc=y#v=onepage&q&f=false (accessed 23 July 2023).

36. Tembely M, Vadillo D, Dolatabadi A, Soucemarianadin A. 2018 On the numerical modeling of FENE-CR viscoelastic droplet impact dynamics by the volume of fluid method. In *ENGINEERING* pp. 7–10 (doi:[10.20944/preprints201807.0265.v1](https://doi.org/10.20944/preprints201807.0265.v1))
37. Jiang X, Xu E, Wu G, Li HZ. 2020 Drop impact on superhydrophobic surface with protrusions. *Chem. Eng. Sci.* **212**, 1–25, 115351. (doi:[10.1016/j.ces.2019.115351](https://doi.org/10.1016/j.ces.2019.115351))
38. V V S Vara Prasad G, Dhar P, Samanta D. 2021 Magneto-elastic effect in non-Newtonian ferrofluid droplets impacting superhydrophobic surfaces. *Langmuir* **37**, 1–10. (doi:[10.1021/acs.langmuir.1c00885](https://doi.org/10.1021/acs.langmuir.1c00885))
39. V V S Vara Prasad G, Dhar P, Samanta D. 2023 Triggering of electro-elastic anti-superhydrophobicity during non-Newtonian droplet collision. *Proc. R. Soc. A* **479**, 20220612. (doi:[10.1098/rspa.2022.0612](https://doi.org/10.1098/rspa.2022.0612))
40. Khurana G, Sahoo N, Dhar P. 2019 Post-collision hydrodynamics of droplets on cylindrical bodies of variant convexity and wettability. *Phys. Fluids* **31**. (doi:[10.1063/1.5064799](https://doi.org/10.1063/1.5064799))
41. Lee JB, Derome D, Dolatabadi A, Carmeliet J. 2016 Energy budget of liquid drop impact at maximum spreading: Numerical simulations and experiments. *Langmuir* **32**, 1279–1288. (doi:[10.1021/acs.langmuir.5b03848](https://doi.org/10.1021/acs.langmuir.5b03848))
42. Yoon I, Chergui J, Juric D, Shin S. 2023 Energetics of spreading droplets and role of capillary waves at low Weber numbers below 10. *Phys. Fluids* **35**. (doi:[10.1063/5.0138378](https://doi.org/10.1063/5.0138378))
43. Zhang B, Sanjay V, Shi S, Zhao Y, Lv C, Feng XQ, Lohse D. 2022 Impact forces of water drops falling on superhydrophobic surfaces. *Phys. Rev. Lett.* **129**, 104501. (doi:[10.1103/physrevlett.129.104501](https://doi.org/10.1103/physrevlett.129.104501))
44. Tazikheh Lemeski A, Seyyedi SM, Hashemi-Tilehnoee M, Naeimi AS. 2024 Influence of triangular obstacles on droplet breakup dynamics in microfluidic systems. *Sci. Rep.* **14**, 1–14. (doi:[10.1038/s41598-024-63922-y](https://doi.org/10.1038/s41598-024-63922-y))
45. Murugadoss K, Dhar P, Das SK. 2017 Role and significance of wetting pressures during droplet impact on structured superhydrophobic surfaces. *Eur. Phys. J. E* **40**, 1–10. (doi:[10.1140/epje/i2017-11491-x](https://doi.org/10.1140/epje/i2017-11491-x))
46. Prasad GVVSV. 2025 Droplet impact and splitting hydrodynamics on superhydrophobic wedges (v2.3.4). Zenodo (doi:[10.5281/zenodo.14736529](https://doi.org/10.5281/zenodo.14736529))
47. Prasad G. 2025 DROP_WEDGE https://github.com/varaprasadgudlavalleti/DROP_WEDGE/